

N -Ink Printer Characterization with Barycentric Subdivision

Vahid Babaei, and Roger D. Hersch

Abstract—Printing with a large number of inks, also called N -ink printing, is a challenging task. The challenges comprise spectral modelling of the printer, color separation, halftoning, and limitations of the amount of inks. Juxtaposed halftoning, a perfectly dot-off-dot halftoning method, has proven to be useful to address some of these challenges. However, for juxtaposed halftones, prediction of colors as a function of ink area-coverages has not yet been fully investigated. The goal of this paper is to introduce a spectral prediction model for N -ink juxtaposed-half-tone prints. As the area-coverage domain of juxtaposed inks forms a simplex, we propose a cellular subdivision of the area-coverage domain using barycentric subdivision of simplexes. The barycentric subdivision provides algorithmically straightforward means to design and implement an N -ink color prediction model. Within the subdomain cells, the Yule-Nielsen spectral Neugebauer model is used for the spectral prediction. Our proposed model is highly accurate for prints with a large number of inks while requiring a relatively low number of calibration samples.

Index Terms— Printer characterization, multi-channel printing, cellular Yule-Nielsen, color prediction model, spectral modeling, interpolation, simplex, barycentric subdivision, point location problem, multi-material 3D print

INTRODUCTION

MULTI-CHANNEL printing or N -ink printing refers to printing processes with more than 4 inks [1-5].

There are various motivations for N -ink printing. The main purpose is to expand the color gamut of CMYK prints. Spectral reproduction is another objective, which aims at obtaining an accurate color reproduction under more than one viewing condition [6]. Synthesizing smooth images with low graininess also requires adding new inks, such as light cyan and light magenta, to the palette of the printer. Additional inks can also be used as spot colors. Spot colors are very popular in the packaging industry. Recently, an N -ink process for printing with metallic inks has been proposed [7].

N -ink printing faces several challenges. The first challenge is the color characterization of an N -ink printer. Printer characterization establishes a relationship between area-coverages of inks and the resulting printed color. For a set of printer control-values, *forward* characterization

determines the reflectance spectrum. There are mainly two approaches for printer characterization. The first one is a black-box approach relying on color measurements of printed samples and on interpolation to create relationships between colors and amounts of inks [8]. The second approach relies on *spectral prediction models* that account for the interaction of light, paper and ink halftones [9]. The parameters of the spectral prediction models are usually derived from the *calibration set*, a set of measured color samples. The challenge in calibration of an N -ink printer resides in the number of required measurements. When increasing the number of inks, the size of the calibration set grows rapidly, usually at an exponential rate.

Another obstacle to N -ink printing is the total area-coverage limit. In a printing setup, depending on the substrate, the inks and the printing technology, only a limited amount of ink can be deposited on a selected region. With an N -ink printer, we cannot superpose a large number of inks at their full area-coverages. Exceeding the total ink-limit can result in deteriorated image quality, ink blotting or mechanical malfunction of the printer.

Halftoning complexity also increases with the number of inks. Because of moiré artifacts, classic clustered-dot methods allow at most 4 ink-half-tone layers to be laid out on top of each other. Recent efforts try to design moiré-free clustered-dot N -ink screens [10, 11]. Although error diffusion halftoning can avoid moiré, it is not suitable for printing systems that require clustered dots.

Recently, Babaei and Hersch proposed a juxtaposed halftoning method that places different inks¹ next to each other without overlap [12]. Discrete-line juxtaposed halftoning is a look-up table based halftoning method. Each screen element is a parallelogram composed of discrete line segments placed side by side (see Figure 7). Each discrete line segment has a rational thickness offering subpixel precision. Discrete-line halftoning is very efficient as any color screen can be synthesized

¹ In this paper we use the term “ink” in a broad sense, sometimes conveying the meaning of the term “colorant”. A colorant usually refers to the printer ink, to the superposition of inks and to the unprinted substrate. The number of colorants in a halftone depends on the number of inks and their superpositions. In standard CMY printing, the three inks yield the 8 well-known Neugebauer colorants (also known as Neugebauer primaries). In juxtaposed halftoning, N inks along with the substrate produce $N + 1$ colorants. If we apply juxtaposed halftoning for printing with standard CMY inks, the 8 Neugebauer primaries are formed by the inks, the ink superpositions and the paper. These Neugebauer primaries are then placed side by side within a screen element.

instantly by relying on a library of only black and white screen elements. Therefore, as many colorants as desired can be juxtaposed within a single screen-element.

The main purpose of juxtaposed halftoning method is to enable printing with inks that cannot be superposed. Metallic inks, fluorescent inks and pearlescent inks are examples of such *non-standard* inks. Discrete-line juxtaposed halftoning is also appropriate for printing with more than three, not necessarily opaque inks (N -ink printing). It lifts the constraint on the number of inks per *single* halftone screen and allows each ink to take a freely chosen area-coverage. In addition, since the ink halftones are laid out side-by-side, it inherently avoids the total ink limit, and moiré due to superposition of ink-halftones.

This paper introduces a new spectral prediction model for the N -ink color characterization of a printer. Our focus is on the characterization of N juxtaposed-ink prints. The area-coverages domain of N juxtaposed colorants form an $(N - 1)$ -dimensional simplex. Inspired by the cellular Yule-Nielsen spectral Neugebauer model for conventional prints, we develop a cellular subdivision of the ink area-coverage domain relying on the barycentric subdivision of the simplexes. Our key insight is that the barycentric subdivision provides an algorithmically straightforward means to devise and implement an N -ink spectral printer model. For N juxtaposed inks, with $2^N - 1$ calibration samples, our proposed model offers an accuracy superior to the accuracy of the nominal Yule-Nielsen spectral Neugebauer model.

FORWARD CHARACTERIZATION OF N -INK PRINTERS

A. Yule-Nielsen spectral Neugebauer model and its variants

Various spectral printer models have been developed in recent decades. Most of them are based on the well-known Neugebauer model [13]. The Neugebauer model predicts the CIEXYZ-color of a given halftone by convex interpolation of the CIEXYZ colors of all participating colorants. Assuming that halftone screen dots of different ink layers are laid out independently one from another, which is an acceptable assumption for classic halftoning methods [14, 15], printing N superposed ink-layers yields 2^N possible colorants whose area coverages can be computed by Demichel equations [9, 15, 16]. In the case of a classic CMY print, the halftone is composed of the 8 colorants, also known as the Neugebauer primaries: white, cyan, magenta, yellow, blue, green, red and black. In order to calculate the area-coverages of the colorants as a function of the amount of inks, we use the Demichel equations.

There have been important improvements of the Neugebauer model. Yule and Nielsen [17] introduced a

nonlinear relationship between the predicted color of a single-ink halftone and the colors of the ink and the paper. The nonlinear relationship is a power function and accounts for the optical dot-gain. The exponent n of the power function is usually fitted using a set of measured halftone patches. Viggiano [18] extended the Yule-Nielsen equation in order to predict the spectral reflectance $R(\lambda)$ of a halftone, yielding the well-known Yule-Nielsen modified Spectral Neugebauer (YNSN) model:

$$R(\lambda) = \left(\sum_i a_i \cdot R_i(\lambda)^{\frac{1}{n}} \right)^n \quad (1)$$

where $R_i(\lambda)$ expresses the spectral reflectance of colorant i , a_i expresses its area coverage, the exponent n is the Yule-Nielsen n -value and λ stands for the wavelength of light.

The prediction accuracy of the YNSN model depends on how accurately we estimate the *effective* area-coverages a_i of the contributing colorants. The effective area coverage is the area coverage of a colorant after accounting for the dot gain. We can use the nominal area-coverages, thereby obtaining the *nominal* YNSN model. Depending on the printer's precision, the nominal model can produce significant prediction errors. To compensate for the dot gain, *ink-spreading models* calculate effective area-coverages of inks. In its simplest form, an ink-spreading model relies on a curve that maps nominal to effective area-coverages for each single ink. These curves are obtained by linear interpolation between fitted area-coverages of halftones printed on paper. Such a model is known as *independent ink-spreading model*. Hersch and Cr  t   [19] developed a general ink-spreading model that accounts for different superposition conditions, called the *superposition-dependent ink-spreading model* [9].

The *cellular* YNSN model has been proposed in order to increase the accuracy of the YNSN model [20, 21]. The cellular model divides the ink area-coverage domain into several subdomains. The YNSN model is then applied inside each subdomain. The new primaries for the cellular YNSN model are the reflectances of subdomain vertices. As each subdomain spans a smaller subset of the color space, the model provides more accurate predictions.

Figure 1 illustrates the cellular YNSN model for three inks. Subdomains are created by dividing the CMY area-coverage unit-cube into 8 subcubes, formed by combinations of 0%, 50% and 100% area-coverages of the cyan, magenta and yellow inks. With such a subdivision, the number of primary reflectances increases from 8 to 27.

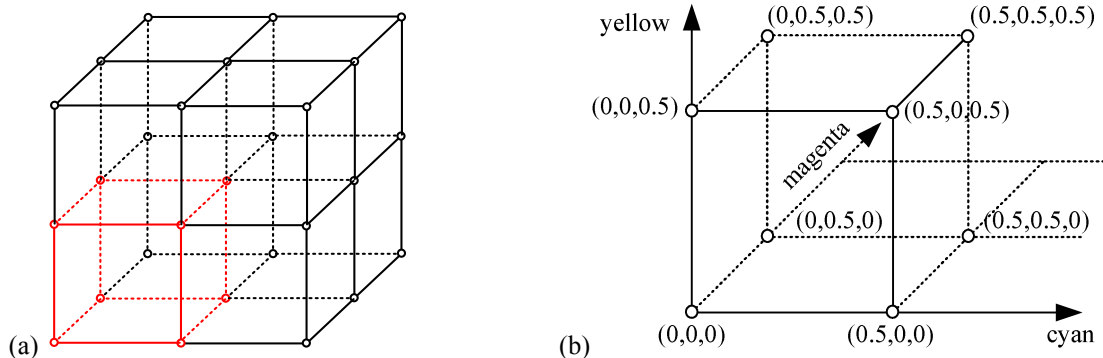


Figure 1. (a) The subdivision of the unit cube that represents the area-coverages of cyan, magenta and yellow inks. (b) The area-coverages of the vertices of one of the 8 subcube cells.

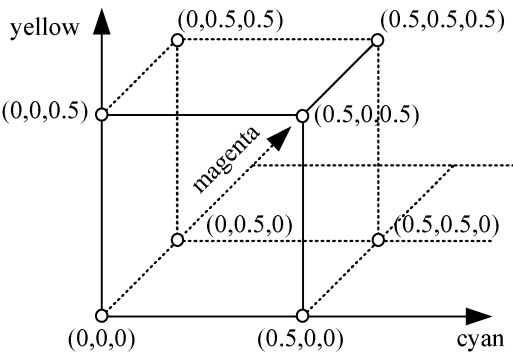
We take the following steps in order to predict the reflectance of a halftone with a given ink area-coverage. First, the circumscribing subcube to the considered halftone is determined according to the halftone’s nominal area coverage. Then, the ink area-coverages normalized with respect to the subcube vertices are calculated. Applying the Demichel equations on the normalized ink area-coverages, the normalized area-coverages of the 8 cellular primaries are then found. Along with the 8 subcube vertex reflectances these normalized area-coverages are used in the YNSN equation (Equation 1) to obtain the reflectance of the halftone.

Another important spectral prediction model is the *two-by-two dot-centering* model [22, 23]. Instead of estimating the effective area-coverage of different colorants in the halftone, it takes into account all possible two-by-two pixel configurations within a given halftone. The model then uses the YNSN equation, with the primaries expressing the reflectances of each two-by-two pattern and the weights expressing the relative frequency of each corresponding pattern. For transparent inks, the *predictive two-by-two* model [24] estimates the whole calibration set using a measured subset of the two-by-two calibration samples. This method achieves almost the same accuracy as the original two-by-two model by requiring only 10% of two-by-two calibration samples.

B. N -ink printer models

An N -ink spectral prediction model predicts the spectra of halftones made of maximum N inks. When the number of inks grows, the size of the calibration set for the characterization of the printer also grows, usually at an exponential rate. This is the main challenge for N -ink spectral printer modelling. A possible solution for the N -ink printer characterization is the *subgamut characterization* [5]. Subgamut characterization categorizes the inks into several groups each one with a small number of inks. Each group (subgamuts) is separately characterized. This leads to less calibration patches compared with a full-blown N -ink printer model. However, there is not a unique way for selecting the ink groups.

For example, consider an 8-ink printer. An 8-ink model predicts the halftones formed by any number of different inks. Subgamut characterization, instead, might form 4-



ink subgamuts and calibrate a 4-ink prediction model for each subgamut. Although we usually choose a subset of the 70 possible 4-ink groups to decrease the size of the calibration set, it is not clear how to select the groups. The 4-ink subgamut characterization is also not able to predict halftones formed by groups of 5 or more inks. Because of the spectral redundancy of conventional inks, groups of more than 4 inks don’t usually contribute to the spectral variability. Nevertheless, combinations of a large number of inks might improve other print attributes or become necessary for printing with unconventional materials.

There have been a few efforts for characterizing an N -ink printer. Taplin and Berns [1] establish a six-ink color prediction model based on the independent ink-spreading YNSN model. They limit the total area-coverage of halftones to 300%. In another work, Chen *et al.* [2] use the cellular YNSN model for a six-ink printer. For each single ink, they find the two best cellular primary locations between 0% 100% area-coverage. They also estimate the cellular primaries that are not printable due to the total ink-limit. Bastani *et al.* [3] also proposed an 8-ink cellular YNSN model. By limiting the total area-coverage, they reduce the number of required calibration samples. These models are all limited to classic halftoning methods where the different ink layers are partially superposed.

C. Spectral prediction of juxtaposed halftones

The application of the nominal YNSN model for the spectral prediction of N juxtaposed colorants is straightforward. N spectrally measured colorants are sufficient for the calibration step. There is no established ink-spreading model for juxtaposed halftoning that could compute the physical dot-gain of the individual colorants and the extent of their possible overlap. Existing ink-spreading models rely on the statistically-independent superposition of ink layers. They are therefore not applicable to juxtaposed halftones.

The two-by-two dot-centering spectral prediction model [22] enables capturing the reflectance of slightly overlapping colorants and is therefore appropriate for predicting the color of juxtaposed halftones. Babaei and Hersch [23] used the two-by-two dot-centering model and its predictive counterpart for the prediction of discrete-line juxtaposed halftones. These models offer high

prediction accuracies and outperform the nominal YNSN model. However, the backward characterization of the two-by-two models is a very difficult problem [7].

The cellular YNSN is a popular spectral prediction model for conventional halftones. In this paper, we propose to extend the cellular YNSN model for N -colorant juxtaposed halftones. The sum of area-coverage of inks in a juxtaposed halftone is equal to 1. This implies that the cellular model for juxtaposed halftones must be implemented in simplexes instead of easy-to-manipulate cubes as in the case of conventional halftones. The readers might find it useful to consult Appendix A where we develop the necessary mathematical background for the next section.

CELLULAR PREDICTION MODEL FOR JUXTAPOSED HALFTONES

Similar to the cellular YNSN model for standard prints, the domain of area-coverages of juxtaposed inks can be divided into smaller subdomains. In a printing setup that allows the superposition of inks, each ink's area-coverage can take a value in the interval $[0, 1]$. In a juxtaposed print, the sum of all area-coverages should be equal to 1. From a geometric viewpoint, when ink superposition is allowed the area-coverage domain for N inks corresponds to an N -cube, i.e. a cube in N dimensions. When the inks are juxtaposed, the area-coverages of N inks correspond to an $(N - 1)$ -dimensional standard simplex. Figure 2 shows this interpretation for $N = 2$ and $N = 3$. For a two-ink print with ink superposition, the domain of area coverage is the unit square, i.e. a 2-cube (Figure 2a). The area-coverages of two juxtaposed inks (e.g. a colored ink and paper) vary along a line segment, i.e. a 1-simplex (Figure 2b). For three superposed inks, their area coverages can take the values bounded by the unit cube (Figure 2c). In juxtaposition, e.g. two colored inks and the white paper, the area-coverage of three inks spans a triangle, i.e. a 2-simplex (Figure 2d).

We must consider two questions when designing a cellular prediction model for juxtaposed inks. The first question is how to choose the location of new cellular primaries in the area-coverage simplex. The second question is how to select the subdomains within which the YNSN model interpolates between cellular primaries. Concerning the first question, there are two main considerations. First, we are interested in the minimum number of cellular primaries. Second, the new primaries in the cellular YNSN model must account for the effects that are not captured by the nominal YNSN model. Because of the dot gain, the borders of neighboring colorants in a juxtaposed halftone are not perfectly separated and produce effects that cannot be represented with single colorants. Therefore, each ink-combination needs to be represented by a new primary. For a set of inks, the new cellular primaries must represent all possible ink-juxtapositions. As the domain of area-coverages of any set of juxtaposed inks forms a simplex, we can set the barycenter of the original simplex and the barycenter of each of its faces as cellular primaries.

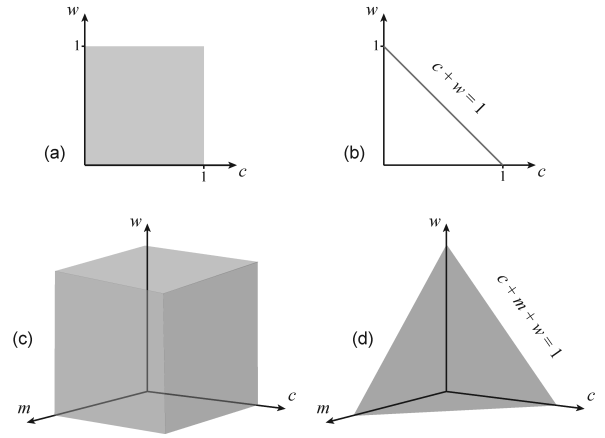


Figure 2. The domain of area-coverages in superposition prints (left) and in juxtaposed prints (right). The top row corresponds to a 2-ink print and the bottom row to a 3-ink print.

For example, consider a three-colorant juxtaposed print formed by three colorants, e.g. white paper, cyan and magenta (Figure 3). One cellular primary included in all subdivisions is the barycenter of the three vertices (\mathbf{p}_{012}). We also consider the barycenters of all two and one-ink faces of the simplex as other cellular primaries. This results in 1 three-colorant barycenter plus 3 two-colorant barycenters which together with the 3 colorant-vertices (barycenters of 0-faces) yield 7 cellular primaries. Similarly, for an N -ink juxtaposed system that forms an $(N - 1)$ -simplex, using the binominal theorem, we can verify that this approach requires

$$\binom{N}{1} + \binom{N}{2} + \dots + \binom{N}{N} = 2^N - 1 \quad (2)$$

cellular primaries among which $\binom{N}{1} = N$ primaries are the ink-vertices.

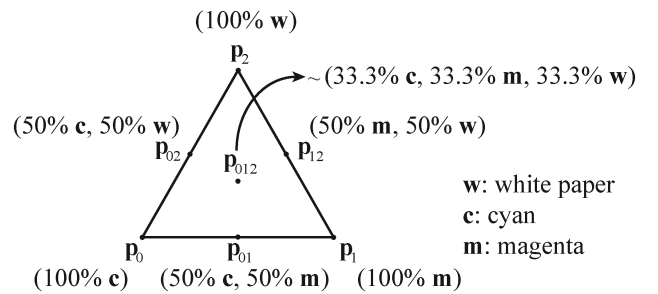


Figure 3. Locations of the cellular primaries in a 3-ink juxtaposed print. For 3 inks, we need 7 cellular primaries. In parentheses, we give an example with colorants cyan, magenta and white.

Having selected the cellular primaries, the second question was how to choose the subdomains within which the YNSN model interpolates between cellular primaries. Given a test point, the answer is straightforward for the cellular YNSN model for standard prints: we choose the smallest subcube that includes the test halftone (see Figure 1). In cellular simplexes, however there is not a unique way of choosing a subdomain. In a simple

experiment with only 3 inks, Figure 4 shows a point that represents a halftone of cyan (37%), magenta (22%) and red (41%) inks. As can be seen, a point inside a cellular subdivided triangle can be interpolated within different subdomains. The reproduction accuracy depends on the interpolation region. To compare, we estimate the reflectance of this point by linearly interpolating within different regions, each one defined by different cellular primaries. The RMS error between the predictions and the measured reflectance is shown in Figure 4.

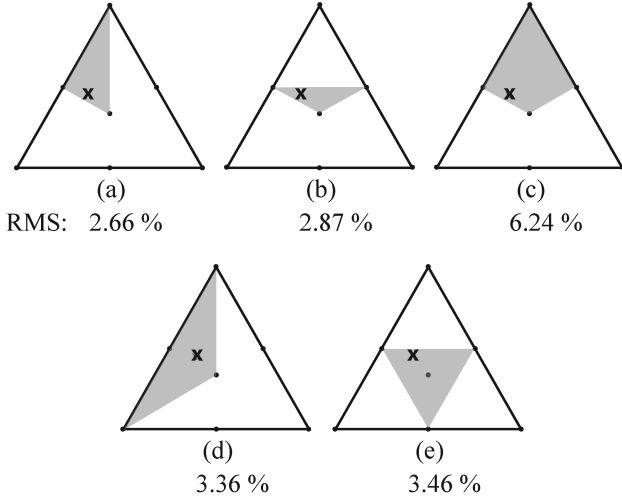


Figure 4. A single point can be interpolated within regions defined by different cellular primaries. The RMS prediction error is given for the printer described in Section IV.

The cellular subdivisions according to Figure 4 (c), (d) and (e) give the largest interpolation errors. They all use cells that have large areas compared to the cells in (a) and (b). Moreover, Figure 4 (c) uses 4 primaries and Figure 4 (e) does not use the three-ink barycenter primary.

One reasonable option is to find the smallest subdomain that circumscribes the test point, similar to Figure 4 (b). However, this *point-location problem* is known to be very computationally expensive in high dimensions [25]. As it must compute the colors of millions of halftones, a forward prediction model should be fast. We are therefore interested in a subdivision that: i) assigns a subdomain to any test point of any dimension quickly and without ambiguity, ii) ensures that subdomains have small areas, and iii) includes the barycenter of N ink-vertices (unlike Figure 4 (e)).

The first barycentric subdivision of a standard simplex (Appendix A) provides us with such desired properties. For three juxtaposed inks, Figure 4 (a) corresponds to this subdivision. As stated in the Appendix, the barycentric subdivision divides a q -simplex (i.e. a simplex with $q + 1$ vertices) into a family of $(q + 1)!$ q -subsimplices (see Figures 10 and 11). Let us review the algorithm for finding the subsimplex circumscribing a given point within a subdivided simplex. This algorithm is a direct result of Corollary 1 in Appendix A. We carry out the following steps:

(i) Input are t_0, t_1, \dots, t_q , the barycentric coordinates of point \mathbf{x} relative to the simplex vertices $\mathbf{p}_0, \mathbf{p}_1, \dots, \mathbf{p}_q$.

Hence, $\mathbf{x} = t_0 \mathbf{p}_0 + t_1 \mathbf{p}_1 + \dots + t_q \mathbf{p}_q$. In our color prediction framework, t_0, t_1, \dots, t_q are the nominal area coverages of the halftone \mathbf{x} . Also, $\mathbf{p}_0, \mathbf{p}_1, \dots, \mathbf{p}_q$ correspond to the area coverages of the $q + 1$ fulltone colorants.

(ii) Order the barycentric coordinates, such that $t_{i_0} \geq t_{i_1} \geq \dots \geq t_{i_q}$.

(iii) The cellular primaries are:

- \mathbf{p}_{i_0} , barycenter of the 0-face of \mathbf{p}_{i_0} ,
- $\mathbf{p}_{i_0 i_1}$, barycenter of the 1-face of $\mathbf{p}_{i_0} \mathbf{p}_{i_1}$,
- ...
- $\mathbf{p}_{i_0 i_1 \dots i_q}$, barycenter of the q -face of the simplex, i.e. the barycenter of the initial simplex $\mathbf{p}_{i_0} \mathbf{p}_{i_1} \dots \mathbf{p}_{i_q}$.

Using this algorithm, given the barycentric coordinates relative to the vertices of the original simplex, the circumscribing subsimplex is found quickly. Computationally, it is as fast as sorting the vector of area-coverages of the test halftone. Consider for example Figure 5 that is a more detailed instance of Figure 4 (a). Recall that the test point shown at position \mathbf{x} is a halftone of cyan (37%), magenta (22%) and red (41%) inks. From Corollary 1 (i) of the Appendix, we know that the 2-simplex \mathbf{cmr} can be divided into $3!$ 2-subsimplices, each characterized by a double inequality. The inequality $t_r \geq t_c \geq t_m$ characterizes the highlighted subsimplex that encompasses the halftone \mathbf{x} , where $t_r = 0.41$, $t_c = 0.37$ and $t_m = 0.22$ are the barycentric coordinates of point \mathbf{x} with respect to the \mathbf{cmr} simplex, i.e. $\mathbf{x} = t_r \mathbf{r} + t_c \mathbf{c} + t_m \mathbf{m}$. With the algorithm described above, we find the cellular primary vertices of the circumscribing subsimplex to \mathbf{x} , i.e. $\mathbf{r} (\mathbf{p}_{i_0})$, $\mathbf{cr} (\mathbf{p}_{i_0 i_1})$ and $\mathbf{cmr} (\mathbf{p}_{i_0 i_1 i_2})$ in the present example.

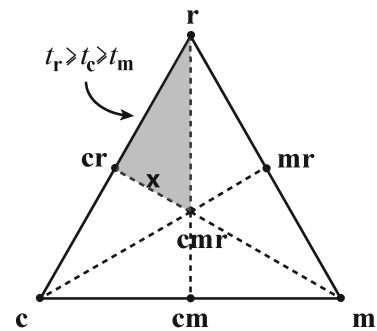


Figure 5. A single point \mathbf{x} with barycentric coordinates $t_r \geq t_c \geq t_m$ has to be interpolated within the corresponding highlighted subsimplex defined by cellular primaries \mathbf{r} , \mathbf{cr} and \mathbf{cmr} .

The area-coverage of a juxtaposed halftone represents its barycentric coordinates relative to the vertices of the original simplex built by the contributing inks. In order to predict the reflectance of a juxtaposed halftone using the cellular YNSN model, we must calculate its new barycentric coordinates relative to its circumscribing subsimplex. These new barycentric coordinates are then

used as weights in the Yule-Nielsen equation (areas a_i in Equation 1).

Finding the barycentric coordinates inside arbitrary shapes even in 2D can be ambiguous [26]. Thanks to the barycentric subdivision, after the subdivision, every point is inside a (sub)-simplex. Calculating the barycentric coordinates of a point inside a simplex is straightforward. We can construct barycentric coordinates in any dimensions using fractions of hypervolumes. In order to compute the barycentric coordinate of a given point \mathbf{p} relative to a certain vertex \mathbf{x} , we can compute the ratio of the hypervolume of the simplex opposite to \mathbf{x} , and the hypervolume of the whole circumscribing simplex [27]. The simplex opposite to \mathbf{x} is defined by the point \mathbf{p} and all circumscribing simplex points but \mathbf{x} .

A test point inside an N -simplex forms an N -simplex with any set of $(N - 1)$ vertices of that simplex. The barycentric coordinates are therefore the ratios of the unsigned hypervolumes of two N -simplexes. The unsigned volume of a simplex of any dimension is [28]

$$V = \left| \frac{1}{q!} \det[\mathbf{p}_1 - \mathbf{p}_0, \mathbf{p}_2 - \mathbf{p}_0, \dots, \mathbf{p}_q - \mathbf{p}_0] \right| \quad (3)$$

where $\mathbf{p}_0, \mathbf{p}_1, \dots, \mathbf{p}_q$ are q -vectors, that yield a square matrix for determinant calculation. Figure 6 shows a 2D example where a juxtaposed 3-ink halftone is represented with area-coverage vector \mathbf{t} (c, m, y). The barycentric coordinates relative to \mathbf{c}, \mathbf{m} and \mathbf{y} vertices, i.e. c, m and y , are equal to the *areas* of the sub-triangles opposite to \mathbf{c}, \mathbf{m} and \mathbf{y} , i.e. $\mathbf{mty}, \mathbf{cty}$ and \mathbf{ctm} , respectively, normalized by the area of the simplex \mathbf{cmY} .

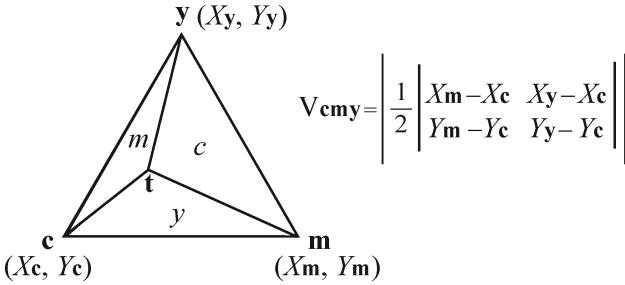


Figure 6. The area-coverage of the halftone represented with the vector \mathbf{t} (c, m, y) is equal to the relative area of the three opposite-side sub-triangles.

RESULTS

In this section, we predict the reflectances of printed samples made of juxtaposed ink-halftones using the nominal YNSN and the cellular simplex models. The juxtaposed halftoning method enables us to directly set the amount of any number of input inks. The assigned ink-amounts are halftoned with the discrete-line juxtaposed halftoning algorithm (see Figure 7). The screen is a 1D superscreen [7, 29] with two subscreens of rational periods $T_1 = 46/7$ and $T_2 = 45/7$ resulting in 92 intensity levels with a line slope of $4/7$. We use the Canon Pixma Pro9500 inkjet printer at 600 dpi with a maximal drop-size and the Canon MP-101 paper for all experiments. The corresponding solid cyan, magenta and

yellow densities are 1.05, 0.80 and 1.11, respectively according to the DIN 16536-2 density standard.

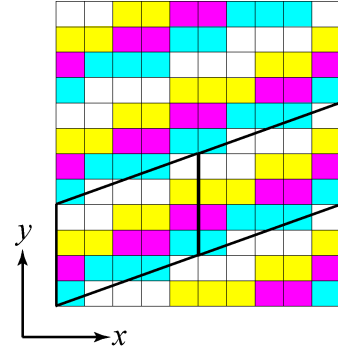


Figure 7. Discrete-line juxtaposed halftoning: a simple example of a screen comprising four colorants with different area-coverages: cyan 25%, magenta 20%, yellow 25% and white 30%. Two instances of the parallelogram screen-element are shown with a solid line. Here the vertical period T is 4 and the line slope is $2/5$.

Although the inks are transparent, we don't allow them to overlap. Hence, each ink is a separate colorant. We use 7 out of the 10 available ink-cartridges for the printer, namely cyan, magenta, yellow, black, red, green and gray which along with the white paper form an 8-colorant juxtaposed system. We measure the spectral reflectances with a Datacolor MF45 spectrophotometer having a $0^\circ:45^\circ$ measuring geometry. The reflectance spectra comprise discrete wavelengths from 380 to 730 nm in 10 nm intervals. Therefore, each halftone reflectance is represented by a 36-vector.

According to Equation 5, the calibration set of the cellular YNSN model is composed of $2^8 - 1 (= 255)$

halftone reflectances among which $\binom{8}{1} = 8$ calibration

samples are the inks at their full area-coverages,

$\binom{8}{2} = 28$ calibration samples are all different 2-ink

halftones where both inks have equal area-coverages,

$\binom{8}{3} = 56$ calibration samples are all different 3-ink

halftones with equal area-coverages and so forth. For the nominal YNSN model calibration, 8 colorants at their full area-coverage are printed and measured.

We design a test set comprising a number of halftones to be measured and compared with the predicted spectra resulting from both the nominal and cellular simplex YNSN models. We include all possible ink-combinations in the test set. We include one test-halftone with random area-coverage for each combination instance. For example, as there are 28 different two-ink combinations, we include 28 two-ink test halftones with the area-coverages of the two inks selected on a random basis. This approach yields a test set of 247 samples, i.e. 255 samples, one per ink combinations, minus the 8 single

colorants. We verified that these 247 samples are well distributed in the color space.

As explained earlier, given the area coverage of a test halftone, we first find the primaries that circumscribe that halftone according to the algorithm described in the previous section. This is performed by sorting the area-coverage vector of the test halftone. We then calculate the barycentric coordinates of the test halftone relative to these primaries and use them in Equation 1 to predict the reflectance. For example, suppose we have a 7-ink test halftone with area coverage vector \mathbf{a} (c, m, y, r, g, w, k), assuming $c \geq m \geq y \geq r \geq g \geq w \geq k$. We know that this point is inside one of $7!$ ($= 5040$) 6-subsimplexes resulting from the barycentric subdivision. The vertices of the circumscribing 6-subsimplex are the barycenters of: **c**, **cm**, **cmy**, **cmyr**, **cmyrg**, **cmyrgw** and **cmyrgwk**

simplexes, i.e. they are formed by halftones with equal amounts of these ink-combinations. These vertices form the cellular primaries that are used for predicting the reflectance spectrum and therefore the color of the considered test halftone.

Table I shows the prediction accuracy of the nominal YNSN, cellular simplex YNSN, the two-by-two dot centering and the predictive two-by-two model using 100 effectively measured calibration samples. Note that the n -values shown in Table I are optimized to give the minimum average ΔE_{94} color-difference between the measured test-halftones and their predicted counterparts. We allowed the n -value to vary between -10 to 10 with 0.1 increments. Values greater than 10 or less than -10 do not change the results significantly [30].

Table I. Prediction accuracy of the nominal and cellular simplex YNSN models for 247 test juxtaposed-halftones printed with a Canon Pixma Pro9500 at 600 dpi, using cyan, magenta, yellow, red, green, gray inks and the white paper.

YNSN model	# calib. set	ΔE_{94}				n -value
		mean	median	quant .95	max	
Nominal	8	2.35	2.06	5.04	7.10	-10
Cellular	255	1.34	1.22	3.15	4.33	-2.5
Two-by-two*	1072	1.24	0.91	3.20	6.91	1.6
Predictive two-by-two*	100	1.41	1.31	3.70	7.10	1.5

* In these experiments the setup is slightly different and instead of the gray ink we used the blue ink.

As it can be seen from Table I, the cellular YNSN model with barycentric subdivision offers significantly more accurate predictions than the YNSN model with nominal area coverages. The nominal YNSN model prediction is already quite accurate. This indicates that the printer is successful in placing halftone dots with effective area-coverages close to nominal area-coverages. The N -ink cellular YNSN model offers a prediction accuracy close to the accuracy obtained by the original two-by-two model with four times less calibration patches and an

primary is shown with the nabla symbol. The choice of inks is arbitrary.

accuracy slightly higher than the predictive two-by-two model, but with 2.5 times the number of calibration patches. In Figure 8, we show the color prediction accuracy of the cellular simplex model for a number of 3-ink juxtaposed halftones depending on their locations in a 2D subdivided simplex.

CONCLUSIONS

In this work, we have presented a new spectral prediction model for N -ink prints made of juxtaposed halftones. It borrows the concept of the cellular subdivision of the ink area-coverage domain which has already been successfully used to predict the color of classic prints. As the domain of the ink area-coverage of juxtaposed halftones forms a simplex, the main challenge resides in determining the location of cellular primary reflectances as well as appropriately subdividing the simplex into subdomains such that the barycentric weights of the primary reflectances can be unambiguously calculated. We have shown that the first barycentric subdivision of simplexes efficiently samples the ink space and offers computationally efficient solutions to find the proper subdomain for each test halftone. The number of calibration samples raises exponentially with the number of inks, but with a modest base of 2. The experiments have shown that the proposed model can predict all combinations of 8-ink prints with a colorimetric accuracy superior to the nominal YNSN

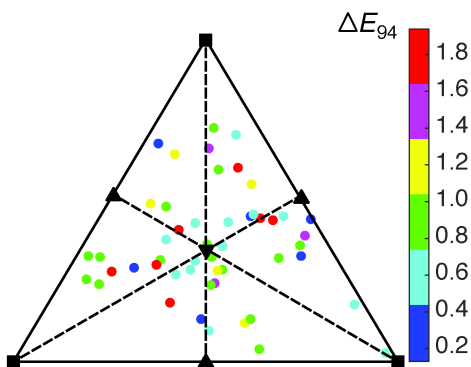


Figure 8. The ΔE_{94} color prediction error for a number of 3-ink halftones predicted with the cellular simplex YNSN. The test halftones are shown with filled circles color-coded according to the prediction accuracy error. The location of the measured calibration samples is also shown with black shapes: The fulltone inks are shown with squares, the two-ink cellular primaries are shown with triangles and the 3-ink cellular

model, very close to the prediction accuracy offered by the two-by-two dot-centering model.

In the future, we can explore other subdivision strategies. A further subdivision of an already subdivided simplex might increase the prediction accuracy. We can also consider an adaptive subdivision strategy where subsimplexes with lower prediction accuracy are further subdivided.

We expect that the barycentric subdivision of the ink space will be advantageous for printing with unconventional inks, such as metallic or iridescent inks. It can also be useful in predicting other appearance attributes, such as spatially varying BRDFs [31]. Given the fact that any material mixture, e.g. multi-material 3D prints, can be represented with simplexes, we believe this method can find applications beyond color or appearance reproduction.

APPENDIX A: MATHEMATICAL BACKGROUND

In this section, we review the necessary mathematical background for building the spectral prediction model for N juxtaposed inks. More detailed explanations can be found in almost every standard textbook on Algebraic Topology, see for example [32, 33].

Definition 1. The points $\mathbf{p}_0, \mathbf{p}_1, \dots, \mathbf{p}_q$ in \mathbf{R}^k forming an ordered set are *geometrically independent* (or *affine independent*) if $\mathbf{p}_1 - \mathbf{p}_0, \mathbf{p}_2 - \mathbf{p}_0, \dots, \mathbf{p}_q - \mathbf{p}_0$ is a linearly independent subset of \mathbf{R}^k .

Definition 2. Let $\mathbf{p}_0, \mathbf{p}_1, \dots, \mathbf{p}_q$ be geometrically independent points of \mathbf{R}^k . The convex set spanned by these points is a q -simplex (σ^q) in \mathbf{R}^k and the points $\mathbf{p}_0, \mathbf{p}_1, \dots, \mathbf{p}_q$ are called the *vertices* of the simplex.

The parameter q is referred to as the *dimension* of the simplex.

A simplex is called a *standard simplex* if its vertices are the points

$$\begin{aligned} \mathbf{p}_0 &= (1, 0, 0, \dots, 0) \\ \mathbf{p}_1 &= (0, 1, 0, \dots, 0) \\ &\vdots \\ \mathbf{p}_q &= (0, 0, 0, \dots, 1). \end{aligned} \quad (4)$$

The *face* of a simplex is a simplex whose vertices are a subset of the vertices of the original simplex. If the simplex τ is a face of simplex σ but not equal to σ , we call τ a *proper face* of σ and denote it by $\tau < \sigma$. Vertices of the simplex are its 0-faces, its edges are its 1-faces. The $(q - 1)$ -faces of a q -simplex are called the *facets* of the simplex.

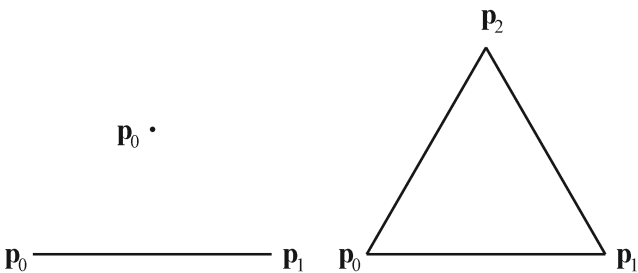


Figure 9. The 0, 1 and 2-dimensional simplexes correspond to a point, a line segment and a triangle, respectively.

Figure 9 shows examples for the first three simplexes. A 0-simplex and a 1-simplex in Euclidean space \mathbf{R}^k are simply a point and a line-segment in that space, respectively. A 2-simplex and a 3-simplex are a triangle and a tetrahedron in \mathbf{R}^k where k is at least 2 and 3, respectively.

Definition 3. For any point \mathbf{x} in a q -simplex, there exists a unique $(q + 1)$ -tuple of real numbers (t_0, t_1, \dots, t_q) called the *barycentric coordinates* of \mathbf{x} relative to the simplex vertices $\mathbf{p}_0, \mathbf{p}_1, \dots, \mathbf{p}_q$ where

$$\left\{ \begin{array}{l} \mathbf{x} = \sum_{j=0}^q t_j \mathbf{p}_j : 0 \leq t_j \leq 1 \\ \text{for } j = 0, 1, \dots, q \quad \text{and } \sum_{j=0}^q t_j = 1 \end{array} \right\}. \quad (5)$$

Definition 4. The *barycenter* of a q -simplex σ with vertices $\mathbf{p}_0, \mathbf{p}_1, \dots, \mathbf{p}_q$, denoted by b^σ , is defined as

$$b^\sigma = \frac{1}{q+1} (\mathbf{p}_0 + \mathbf{p}_1 + \dots + \mathbf{p}_q). \quad (6)$$

Definition 5. The *first barycentric subdivision* of a q -simplex σ^q is a family of q -simplexes defined inductively for $q \geq 0$:

(i) the barycentric subdivision of a 0-simplex is a 0-simplex.

(ii) if $\varphi_0, \varphi_1, \dots, \varphi_{q+1}$ are the facets of a $(q + 1)$ -simplex σ^{q+1} and if b^σ is the barycenter of σ^{q+1} , then the barycentric subdivision of the σ^{q+1} consists of all $(q + 1)$ -simplexes spanned by b^σ and by q -simplexes resulting from the barycentric subdivision of φ_i ($i = 0, 1, \dots, q + 1$).

Figure 10 shows an example of the barycentric subdivision. On the left, the barycentric subdivision of a 1-simplex line-segment gives two smaller line-segments both with one vertex and the barycenter of the original 1-simplex. On the right, we show the barycentric subdivision of a 2-simplex. Following Definition 5, the 2-simplex has three 1-simplex facets, i.e. line segments $\mathbf{p}_0\mathbf{p}_1$, $\mathbf{p}_1\mathbf{p}_2$ and $\mathbf{p}_2\mathbf{p}_0$. The barycentric subdivision of this triangle consists of all possible triangles spanned by the simplex barycenter, i.e. \mathbf{p}_{012} and the 1-simplexes resulting from the subdivision of all 1-simplex facets, i.e. $\mathbf{p}_0\mathbf{p}_{01}$,

$\mathbf{p}_1\mathbf{p}_{01}$, $\mathbf{p}_1\mathbf{p}_{12}$, $\mathbf{p}_2\mathbf{p}_{12}$, $\mathbf{p}_2\mathbf{p}_{02}$ and $\mathbf{p}_0\mathbf{p}_{02}$. In Figure 11 we show the barycentric subdivision of a 3-simplex, i.e. a tetrahedron in 3-dimensional space.

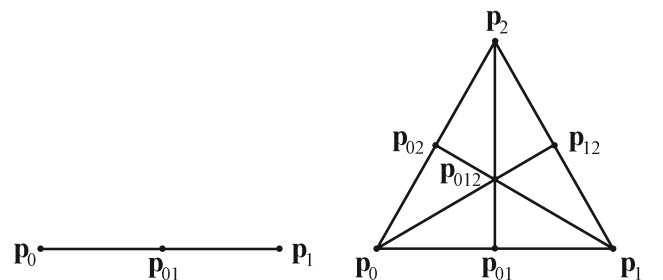


Figure 10. The barycentric subdivision of a 1 and 2-simplex. Note that the barycenter of the original simplex (\mathbf{p}_{01} and \mathbf{p}_{012} for the line segment and the triangle, respectively) is included in all subdivided simplices.

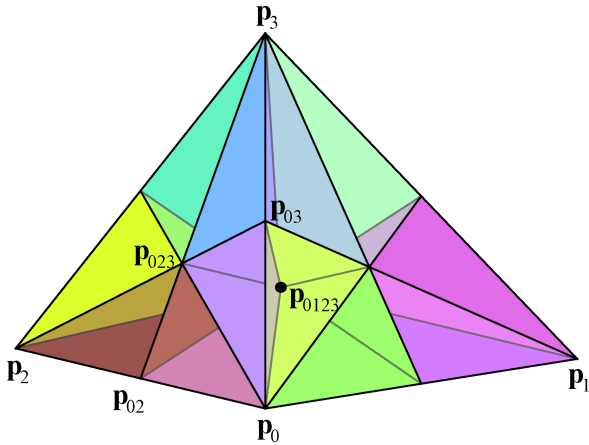


Figure 11. The barycentric subdivision of a 3-simplex, $\mathbf{p}_0\mathbf{p}_1\mathbf{p}_2\mathbf{p}_3$. The barycenter of the 3-simplex, i.e. \mathbf{p}_{0123} is marked with a disk. The 3-simplex has 4 facets: $\mathbf{p}_0\mathbf{p}_1\mathbf{p}_3$, $\mathbf{p}_0\mathbf{p}_2\mathbf{p}_3$, $\mathbf{p}_0\mathbf{p}_1\mathbf{p}_2$ and $\mathbf{p}_1\mathbf{p}_2\mathbf{p}_3$. The subdivision produces 24 3-subsimplices, two of which are $\mathbf{p}_0\mathbf{p}_{02}\mathbf{p}_{023}\mathbf{p}_{0123}$ and $\mathbf{p}_0\mathbf{p}_{03}\mathbf{p}_{023}\mathbf{p}_{0123}$, for example.

The following corollary from the definition of barycentric subdivision is of particular interest. It can be found in the form of an exercise, for example in [32, Exercise 6.6] or in [33, Section 2.1, Exercise 24].

Corollary 1. (i) Each q -simplex resulting from the barycentric subdivision of a q -simplex σ is defined by q inequalities $t_{i_0} \leq t_{i_1} \leq \dots \leq t_{i_q}$ where $t_{i_0}, t_{i_1}, \dots, t_{i_q}$ are the barycentric coordinates relative to σ and (i_0, i_1, \dots, i_q) is a permutation of $(0, 1, \dots, q)$.

(ii) Moreover, every q -simplex of a barycentric subdivision has the vertices $b^{\sigma_0}, b^{\sigma_1}, \dots, b^{\sigma_q}$, where each σ_i is an i -face of σ and $\sigma_0 < \sigma_1 < \dots < \sigma_q$ (recall $\tau < \sigma$ indicates that τ is a proper face of σ). The order of σ_i s in the inequality depends on the order of the barycentric coordinates $(t_{i_0}, t_{i_1}, \dots, t_{i_q})$.

Proof. See [34] for an extensive proof.

The first part of Corollary 1 determines the distinct subsimplices after the barycentric subdivisions expressed as a function of their barycentric coordinates. It shows that the barycentric subdivision of a q -simplex gives exactly $(q + 1)!$ q -simplices. We can verify this in Figures 10 and 11 where the barycentric subdivision of a 1, 2 or 3-simplex gives 2, 6 or 24 1-, 2- or 3-simplices, respectively.

The second part of Corollary 1 determines the circumscribing vertices of each subsimplex. Figure 12 illustrates Corollary 1 for a 2-simplex. The 6 subdivided 2-simplices with barycentric subdivision are characterized with 6 double inequalities. We can list the vertices of each subdivided simplex easily with the help of part (ii) of the corollary. For example, the subdivided triangle characterized by inequality $t_0 \geq t_1 \geq t_2$ has the vertices \mathbf{p}_0 , \mathbf{p}_{01} and \mathbf{p}_{012} . Note that, following Corollary 1 part (ii), \mathbf{p}_0 is the barycenter of the 0-face \mathbf{p}_0 that is the vertex corresponding to the largest element in the

barycentric coordinate (t_0), \mathbf{p}_{01} is the barycenter of the 1-face $\mathbf{p}_0\mathbf{p}_1$ formed by the two vertices corresponding to the two larger elements of the barycentric coordinate (t_0 and t_1) and \mathbf{p}_{012} is the barycenter of the 2-face of simplex $\mathbf{p}_0\mathbf{p}_1\mathbf{p}_2$, which is the simplex $\mathbf{p}_0\mathbf{p}_1\mathbf{p}_2$ itself.

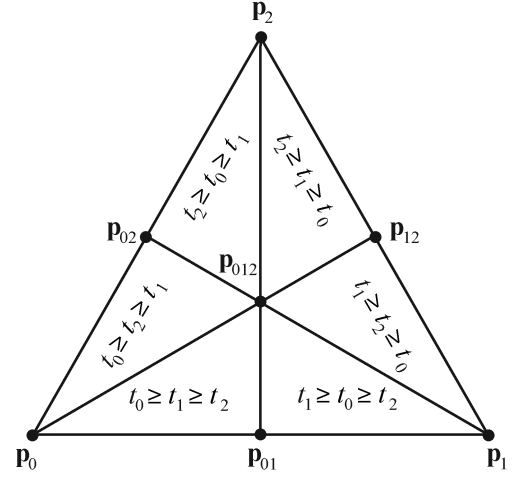


Figure 12. Characterization of each subdivided simplex using the inequalities of the barycentric coordinates.

ACKNOWLEDGEMENTS

The first author gratefully acknowledges the financial support provided by Swiss National Science Foundation (SNSF), grant no. 161843.

References

- [1] L. A. Taplin and R. S. Berns, "Spectral color reproduction based on a six-color inkjet output system," *Proc. IS&T/SID Ninth Color Imaging Conference*, Springfield, pp. 209–213, 2001.
- [2] Y. Chen, R. S. Berns and L. A. Taplin, "Six color printer characterization using an optimized cellular Yule–Nielsen spectral neugebauer model", *Journal of Imaging Science and Technology*, Vol. 48, No. 6, pp. 519–528, 2004.
- [3] B. Bastani, B. Cressmana and M. Shaw, "Sparse cellular Neugebauer model for N-ink printers", *Proc. IS&T/SID 14th Color Imaging Conference*, Scottsdale, pp. 220–223, 2006.
- [4] K. Deshpande, P. Green and M. R. Pointer, "Gamut evaluation of an n-colour printing with the minimum number of measurements," *Color Research and Application Journal*, Vol. 40, No. 4, pp. 408–415, 2015.
- [5] D. Y. Tzeng and R. S. Berns, "Spectral-based six-color separation minimizing metamerism," *Proc. IS&T/SID 8th Color Imaging Conference*, pp. 342–347, 2000.
- [6] P. Urban and R. S. Berns, "Parameter mismatch-based spectral gamut mapping," *IEEE Transactions on Image Processing*, Vol. 20, No. 6, pp. 1599–1610, 2011.
- [7] V. Babaei, Color Reproduction with Juxtaposed Halftoning. Lausanne: Ph.D. dissertation, No. 6703, École Polytechnique Fédérale de Lausanne (EPFL), 2015. Available at <http://library.epfl.ch/theses/>.
- [8] J. Morovič, J. Arnabat, Y. Richard, and A. Albarran, "Sampling optimization for printer characterization by greedy search," *IEEE Transactions on Image Processing*, Vol. 19, No. 10, pp. 2705–2711, 2010.
- [9] M. Hébert and R. D. Hersch, "Review of spectral reflectance models for halftone prints: Principles, calibration, and prediction accuracy," *Color Research and Application*, Vol. 40, No. 4, pp. 383–397, 2015.

[10] Y. Y. Chen, T. Kashti, M. Fischer, D. Shaked, R. Ulichney, and J. P. Allebach, "The lattice-based screen set: A square N-color all-orders moire-free screen set," *IEEE Transactions on Image Processing*, To appear, 2016.

[11] X. Zhang, A. Veis, R. Ulichney, and J. P. Allebach, "Multilevel halftone screen design: Keeping texture or keeping smoothness?," *Proc. ICIP IEEE International Conference on Image Processing*, Orlando, FL, pp. 829–832, 2012.

[12] V. Babaei and R. D. Hersch, "Juxtaposed color halftoning relying on discrete lines," *IEEE Transactions on Image Processing*, Vol. 22, No. 2, pp. 679–686, 2013.

[13] W. Rhodes, "Fifty years of the Neugebauer equations," *SPIE: Neugebauer memorial seminar on colour reproduction*, Vol. 1184, pp. 7–18, 1989.

[14] I. Amidror and R. D. Hersch, "Neugebauer and Demichel: Dependence and independence in n-screen superpositions for colour printing," *Color Research and Application*, Vol. 25, No. 4, pp. 267–277, 2000.

[15] R.D. Hersch, "Demichel equations," *Encyclopedia of Color Science and Technology*, (Ed. R. Luo), Springer, pp 1-4, doi:10.1007/978-3-642-27851-8_21-1.

[16] E. Demichel, *Le procédé*, Vol. 26, pp. 17–21, 26–27, 1924.

[17] J. A. C. Yule and W. J. Nielsen, "The penetration of light into paper and its effect on halftone reproductions," *Proc. TAGA*, Vol. 3, pp. 65–76, 1951.

[18] J. A. S. Viggiano, "Modeling the color of multi-colored halftones," *Proc. TAGA*, pp. 44–62, 1990.

[19] R. D. Hersch and F. Crété, "Improving the Yule-Nielsen modified spectral Neugebauer model by dot surface coverages depending on the ink superposition conditions," *IS&T/SPIE Electronic Imaging Symposium, Conf. Imaging X: Processing, Hardcopy and Applications*, Vol. 5667, p. 434–445, 2005.

[20] Heuberger KJ, Jing ZM, and Persiev S, "Color transformations and lookup tables," *Proceedings of the TAGA/ISCC*, Williamsburg, Virginia, pp. 863–88, 1992.

[21] R. Balasubramanian, "Optimization of the spectral Neugebauer model for printer characterization," *Journal of Electronic Imaging*, Vol. 8, pp. 156–166, 1999.

[22] S. G. Wang, "Two-by-two centering printer model with Yule-Nielsen equation," in *IS&T International Conference on Digital Printing Technologies*, pp. 327–330, 1998.

[23] V. Babaei and R. D. Hersch, "Spectral prediction of juxtaposed halftones relying on the two-by-two dot centering model," *Journal of Imaging Science and Technology*, Vol. 57, No. 4, pp. 040501-1–9, 2013.

[24] V. Babaei, R. Rossier, and R. D. Hersch, "Reducing the number of calibration patterns for the two-by-two dot centering model," *SPIE Electronic Imaging*, Vol. 8292, paper 829208, pp. 1–9, 2012.

[25] F. Preparata and M. Shamos, *Computational Geometry*. Springer-Verlag, 1990.

[26] M. S. Floater, K. Hormann, and G. Kós, "A general construction of barycentric coordinates over convex polygons," *Advances in Computational Mathematics*, Vol. 24, pp. 311–331, 2006.

[27] A. J. Hanson, "Geometry for N-dimensional graphics," in *Graphics Gems IV*. Academic Press, San Francisco, pp. 149–170, 1994.

[28] P. Stein, "A note on the volume of a simplex," *The American Mathematical Monthly*, Vol. 73, No. 3, pp. 299–301, 1966.

[29] V. Babaei and R. D. Hersch, "Reducing auto moiré in discrete line juxtaposed halftoning," *SPIE Electronic Imaging*, Vol. 9395, paper 86520N, pp. 1–9, 2013.

[30] V. Babaei and R. D. Hersch, "Yule-Nielsen based multi-angle reflectance prediction of metallic halftones," *SPIE Electronic Imaging*, Vol. 9395, paper 93950H, pp. 1–10, 2015.

[31] W. Matusik, B. Ajdin, J. Gu, J. Lawrence, H. P.A. Lensch, F. Pellacini, and S. Rusinkiewicz, "Printing spatially-varying reflectance," *ACM Trans. Graphics*, Vol. 28, No. 5, article 128, 9 pages, 2009.

[32] J. J. Rotman, *An Introduction to Algebraic Topology*. Springer, New York, Ch. 2 & 6, 1988.

[33] A. Hatcher, *Algebraic Topology*. Cambridge University Press, 2001.

[34] D. R. Wilkins, "Lecture Notes for Algebraic Topology II, Part II (Sections 3, 4 and 5)" available at: http://www.maths.tcd.ie/~dwilkins/Courses/MA3428/MA3428_Hil2011_PartII.pdf



Vahid Babaei obtained his PhD in Computer Science from Ecole Polytechnique Fédérale de Lausanne (EPFL), where he worked with the group of Prof. R. D. Hersch. He is currently a postdoctoral researcher at the Computational Fabrication Group of Computer Science and Artificial Intelligence Laboratory (CSAIL) in Massachusetts Institute of Technology (MIT). His research interest is in computational fabrication with a focus on appearance reproduction.



Roger D. Hersch received the engineering and PhD degrees from ETH Zurich in 1975 and from EPFL in 1985, respectively. He is a professor of computer science and head of the Peripheral Systems Laboratory at the Ecole Polytechnique Fédérale de Lausanne (EPFL), Switzerland.

He has published more than 150 scientific papers, is the editor of several books, and is inventor or co-inventor in many patent applications. He is interested in novel imaging techniques related to color prediction, color reproduction, artistic imaging, and security printing. He is a fellow of IS&T (Society for Imaging Science and Technology).